Giant exciton oscillator strength and radiatively limited dephasing in two-dimensional platelets - Supplement

Ali Naeem,[1] Francesco Masia,[1] Sotirios Christodoulou,[2] Iwan Moreels,[2] Paola Borri,[1,3] and Wolfgang Langbein[1,*]

[1] *Cardiff University School of Physics and Astronomy, The Parade, Cardiff CF24 3AA, United Kingdom*
[2] *Istituto Italiano di Tecnologia, Via Morego 30, IT-16163 Genova, Italy*
[3] *Cardiff University School of Biosciences, Museum Avenue, Cardiff CF10 3AX, United Kingdom*

(Dated: March 25, 2015)

I. MATERIALS AND METHODS

A. NPL synthesis

Chemicals: Cadmium nitrate tetrahydrate, cadmium acetate dihydrate $Cd(Ac)_2{\cdot}2H_2O$, technical grade 1-octadecene (ODE), oleic acid and sodium myristate were purchased from Sigma-Aldrich. Selenium (Se) mesh 99.99% was purchased from STREM.

Synthesis of cadmium myristate (Cd(myr)$_2$): 5 g (0.02 mol) of sodium myristate was dissolved in 150 mL of methanol by stirring the solution for 1 hour at room temperature. After addition of a solution of 3 g of cadmium nitrate in 10 mL of methanol, a white powder formed which was collected and dried for two days under vacuum.

Synthesis of CdSe nanoplatelets emitting around 515 nm: The investigated NPLs have been synthesized according to the method reported in Ref. 2, albeit using a twice larger Se concentration, and injecting 2.25 times more cadmium acetate, at a temperature of 210°C. In detail, 170 mg of $Cd(myr)_2$ (0.3 mmol), 12 mg of Se and 15 mL of ODE were added in a three-neck flask and degassed under vacuum. The mixture was heated under argon flow to 210°C, and when this temperature was reached, 90 mg of $Cd(Ac)_2$ were swiftly introduced. The mixture was further heated to 240°C and kept at this temperature for 10 minutes. The NPL solution also contained a fraction of spherical quantum dots, which were separated from the NPLs by selective precipitation. After synthesis the average NPLs size and corresponding standard deviation were measured with transmission electron microscopy, evaluating the length and width of 70 particles. The X-ray diffraction pattern was measured on a drop-casted thin film of NPL using miscut silicon substrates.

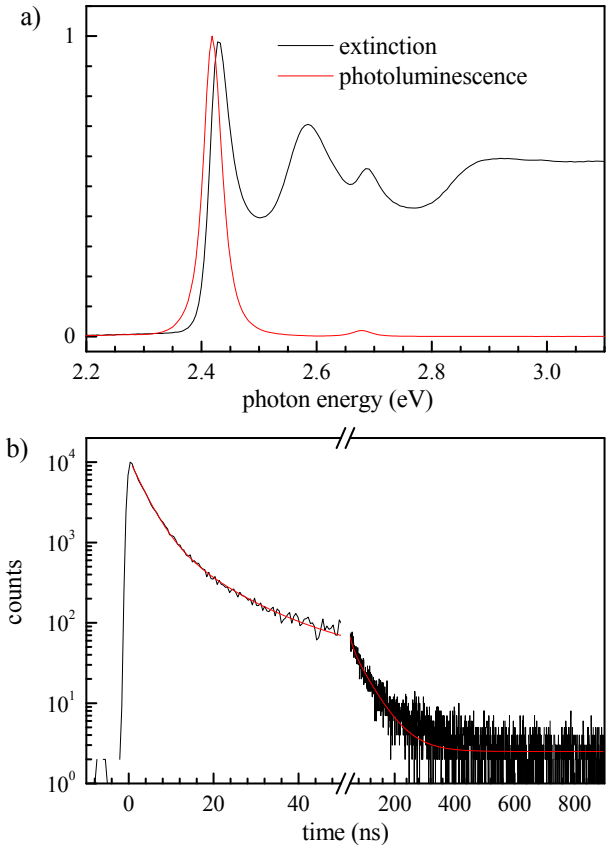

FIG. S1. Optical properties of the investigated CdSe NPL colloid in toluene at room temperature. a) Normalized extinction (black line) and photoluminescence (red line) spectra. b) Time-resolved photoluminescence black line:data, red line: triple-exponential fit yielding the time constants $\tau_1 = 3.36 \pm 0.06$ ns, $\tau_2 = 11.2 \pm 0.4$ ns, $\tau_3 = 61 \pm 2$ ns and amplitudes $A_1 = 9540 \pm 110$, $A_2 = 1530 \pm 111$, $A_3 = 112 \pm 6$.

B. Colloid extinction and photoluminescence

The optical properties of the NPL colloid used to prepare the samples were characterized. Photoluminescence (PL), excited at 400 nm wavelength, and extinction spectra are shown in Fig. S1b. The colloid is dominated by 5.5ML NPLs, but also 4.5ML thick NPLs are visible, having about 5% number fraction as estimated from the heavy hole exciton extinction peak. They are not affecting the FWM in resonance with X_{hh} of the 5.5ML NPLs. The PL is dominated by excitonic emission with a Stokes shift of about 11 meV, and a linewidth of 38 meV. The time-resolved PL is shown in Fig. S1b and was excited with 50 ps pulses at 400 nm with 1 MHz repetition rate and detected using time-correlated single photon counting with a time-resolution of 0.7 ns. It reveals an initial decay time of about 3 ns accounting for 57% of the total

emission, followed by a component with 11 ns accounting for 30%, and 60 ns accounting for 12%.

This dynamics is comparable to reports of the PL dynamics in literature[3]. When a higher time-resolution in employed, also components of faster emission dynamics in the 100 ps range have been reported[7].

C. Sample preparation in polymer

The samples were prepared in the following way. A NPL toluene colloid with 20μM concentration was mixed with a solution of 5% weight polystyrene of average molecular weight 280000 in toluene. The volume ratio of NPL colloid to polystyrene solution was 8 : 2. The resulting solution was drop-cast onto a microscope slide placed on a hotplate at a temperature of 80°C. Four layers of 5μL dropcasts were made on top of each other. Each dropcast was allowed to dry for a few minutes before the next one was applied. A suitable region of the resulting film was cut to a size of approximately $0.5 \times 0.5\,\mathrm{mm}^2$ and squeezed between two 1 mm thick quartz windows of 5 mm diameter using a home-made sample holder. The sample holder was then placed on a hot plate at 120°C for a few seconds and the two quartz windows were further squeezed together to ensure good thermal contact with the sample.

NPL aggregation in the sample could change their dynamics[34] due to Förster-type interactions, typically relevant for distances below 10 nm. To verify that this is not a significant effect in the investigated samples, we have measured the spatial distribution of the NPL in the polymer sample by transmission electron microscopy (TEM). Tiny film fragments were embedded in a super glue drop on a polymeric support, in order to handle the samples to be cut for the cross sectional studies. Sections of about 70 nm were cut with a diamond knife (Diatome) on a Leica EM UC6 ultramicrotome. TEM images were collected by a FEI Tecnai G2 F20 equipped with a field-emission gun (FEG), operating at 200 kV of acceleration voltage and recorded with a 4 Mp Gatan BM UltraScan Charge-Coupled Device (CCD) camera.

A representative high resolution image of a section of the sample is given in Fig. S2. A small fraction shows distances below 10 nm. We do not expect that this type of aggregation significantly influences the dynamics. Lower resolution images reveals some bunching on a micrometer length scale. This might be the origin of the stronger Rayleigh scattering tails observed in the extinction spectra compared to solution measurements.

D. Low-temperature extinction spectra

Low-temperature extinction spectra were measured with a tungsten white-light source and a Ocean Optics HR4000 spectrometer. The transmitted spectral intensity $I_\mathrm{s}(\omega)$ through the sample was measured over a sample region of 20 μm diameter, and compared with a reference transmission $I_\mathrm{r}(\omega)$ at a position without polymer film laterally offset from the sample of about 0.5 mm lateral size and 10 μm thickness. The resulting extinction is given by $\alpha_\mathrm{ext}(\omega) = \ln(I_s/I_\mathrm{r})$ and is shown in Fig. S3a. It resembles the room temperature extinction measured in the colloid shown in Fig. S1a, but is shifted to higher energies due to the temperature dependent band-gap shift. Furthermore, we observe a reduced linewidth of the heavy-hole exciton, attributed to reduced phonon-scattering, similar to other reports in literature[7].

FIG. S2. Transmission electron microscopic image of a sample of CdSe NPL in PS prepared in the same way as the sample studied in the dephasing measurements. The scale bar is shown

E. Extinction fit

The extinction of the NPL ensemble was fitted using a quantum-well absorption model, consisting for each interband transition of the 1s exciton absorption and a continuum edge, with a line-shape

$$p(\omega) = p_\mathrm{X} + \frac{L/\pi}{\gamma_\mathrm{L} + \Delta^2/\gamma_\mathrm{L}} + \frac{A_\mathrm{C}}{2}\left[1 + \mathrm{erf}\left(\frac{\Delta - \omega_\mathrm{B}}{\gamma_\mathrm{C}}\right)\right] \quad (1)$$

where $\Delta = \omega - \omega_0$, with the exciton energy ω_0, the linewidth γ, and the exciton binding energy ω_B. The continuum step height is A_C and the step width is γ_C. The 1s exciton line-shape is modeled by an absorption shape p_X of unity area and an additional broader Lorentzian of width γ_L and area L, accounting for the observed tails attributed to Rayleigh scattering.

The absorption line-shape of a quantum well exciton can be modeled accurately by an asymmetric lineshape taking into account the in-plane localization[4,35]

$$p_\mathrm{X} = \frac{1}{2\eta}\left[1 + \mathrm{erf}\left(\frac{\Delta}{\gamma} - \frac{\gamma}{2\eta}\right)\right]\exp\left(\frac{\gamma^2}{4\eta^2} - \frac{\Delta}{\eta}\right) \quad (2)$$

with the additional parameter η describing the asymmetric broadening by localization. In case the inhomoge-

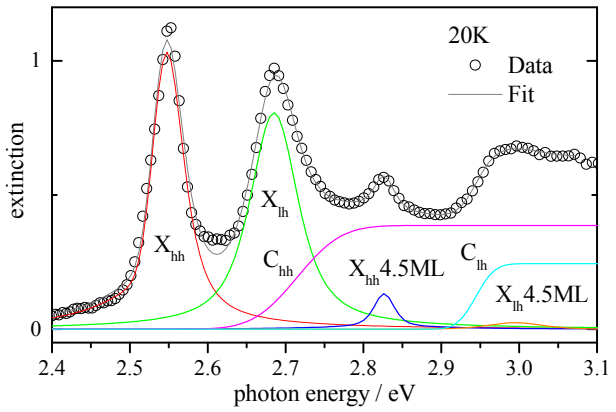

FIG. S3. Measured NPL extinction spectrum (circles) and fit (black line) with its individual components as labeled.

neous broadening is not significant, we use the simpler function

$$p_{\mathrm{X}} = \frac{1}{2\gamma \cosh^2\left(\Delta^2/\gamma^2\right)} \tag{3}$$

with a FWHM of $1.763\,\gamma$, having exponential tails, which was giving better fits than a Gaussian line-shape. For the heavy-hole band we used p_{hh} according to Eq.(2). For the light-hole band instead, we used p_{lh} given by the simpler Eq.(3) since the exciton shows a larger homogeneous broadening due to scattering into the overlapping heavy-hole exciton continuum, as known from quantum wells[36]. The resulting lineshape is

$$\alpha_{\mathrm{ext}}^{5.5\mathrm{ML}} = A_{\mathrm{hh}} p_{\mathrm{hh}} + A_{\mathrm{lh}} p_{\mathrm{lh}} \tag{4}$$

with the weights A_{hh} and A_{lh} of the bands. Since the sample shows a small amount of 4.5ML platelets in both PL and extinction, we have fitted a 4.5ML extinction spectrum at room temperature separately, and added this fit $\alpha_{\mathrm{ext}}^{4.5\mathrm{ML}}$, with an amplitude factor and a rigid energy shift due to the temperature difference, to arrive at $\alpha_{\mathrm{ext}} = \alpha_{\mathrm{ext}}^{5.5\mathrm{ML}} + A_{4.5\mathrm{ML}} \alpha_{\mathrm{ext}}^{4.5\mathrm{ML}}$. The parameters L and γ_L were chosen equal for all bands. The resulting fit to the NPL extinction data at 20K is shown in Fig. S3, showing also the individual components. The corresponding fit parameters with fit error estimates are summarized in Table SI.

It is worth noting that zinc-blende CdSe has an additional interband transition due to the split-off valence band with a separation of about $\Delta_{\mathrm{so}} = 0.39\,\mathrm{eV}$ to the hh and lh band, which results in an additional excitonic transition. Its energy should be shifted by Δ_{so} and by the quantization energy which is expected to be in-between the one of heavy hole and light hole band according to the effective mass being in-between the ones of these bands. We therefore would expect an additional absorption around 3 eV from the split-off 1s exciton, which is close to the fitted position of $\mathrm{C_{lh}}$. This excitonic transition is expected to be significantly broadened by the decay into heavy-hole and light-hole excitons and continua, beyond what was observed for the light-hole exciton.

	hh 5.5ML	lh 5.5ML	hh 4.5ML	lh 4.5ML
L	2.1 ± 0.2			
$\hbar\gamma_{\mathrm{L}}$/meV	0.145 ± 0.017			
$A \times 10^2$meV	4.16 ± 0.2	4.37 ± 0.95	0.38 ± 0.09	0.22 ± 0.05
$\hbar\omega_0$/meV	2536.9 ± 1.5	2685.2 ± 1.6	2826.5 ± 3	2826.5 ± 3
$\hbar\omega_{\mathrm{B}}$/meV	178 ± 34	259 ± 3	-	-
$\hbar\gamma$/meV	21.2 ± 0.9	36.1 ± 2.0	16.6 ± 4	46.1 ± 11
$\hbar\eta$/meV	16.3 ± 2.5	-	-	-
$\hbar\gamma_{\mathrm{C}}$/meV	63 ± 30	27 ± 4	-	-
$A_{\mathrm{C}}\times$meV	9.3 ± 0.5	5.6 ± 1.2	-	-

TABLE SI. Fit parameters with errors of the absorption fit shown in Fig. S3, yielding an $R^2 = 0.99427$.

Changing the NPL thickness, the ratio between Δ_{so} and the exciton binding energies changes. Indeed, the extinction spectra shown in Ref. 2 for NPL of different thickness show a changing shape around $\mathrm{C_{lh}}$. The 7ML NPL has a peak at the expected $\mathrm{X_{so}}$ position, with $\mathrm{C_{lh}}$ being below $\mathrm{X_{so}}$, while the 5ML NPL shows a double step structure with $\mathrm{C_{lh}}$ being above $\mathrm{X_{so}}$. In the 6ML NPL, $\mathrm{X_{so}}$ seems to be be just below $\mathrm{C_{lh}}$, resulting in a flat-top structure. The effect of the split-off exciton therefore might shift the apparent continuum edge to somewhat lower energies, leading to an underestimation of the lh exciton binding energy in the fit.

II. HETERODYNE DETECTED FOUR-WAVE MIXING

A. Transient Four-Wave Mixing

The dephasing time, conventionally called T_2, of an optical transition can be measured experimentally in different ways. The homogeneous width of the spectral absorption is inversely proportional to the dephasing time, thus experiments can be performed either in the time domain to directly address the transient decay of the polarization induced by a pulsed coherent light field or in the spectral domain by measuring the steady-state optical absorption lineshape. Generally, the response of the medium to the incident field depends on the field intensity. For example, only in the linear response limit (i.e. in the first order of the incident field amplitude) the absorption lineshape is Lorentzian with the half-width at half-maximum (HWHM) in angular frequency given by $\gamma = 1/T_2$.

One important limitation of linear spectroscopy in determining the homogeneous lineshape is inhomogeneous broadening within the measured ensemble. In the time domain, this translates into an additional decay rate, sometimes called $1/T_2^*$, of the macroscopic first-order polarization. It is inversely proportional to the inhomoge-

neous spectral width, which in the following is assumed to be Gaussian of standard deviation σ and FWHM $\sigma\sqrt{8\ln 2}$. In strongly inhomogeneously broadened systems ($\gamma \ll \sigma$), linear spectroscopy usually fails in measuring the dephasing time, with the exception of speckle-analysis of the resonant Rayleigh scattering[37,38].

One can isolate a single system from the inhomogeneous ensemble to circumvent the inhomogeneous broadening, and perform linear spectroscopy. However, resonant spectroscopy of this type is typically severely limited by background light, as the directional selection is not valid for single emitters of sizes smaller than the light wavelength. Background light can be suppressed by using e.g. non-resonant excitation as in photoluminescence experiments[39,40], or excitation by an internal waveguide mode[41] or at the Brewster angle. However, even a single emitter can show an effective inhomogeneous broadening due to a slow spectral diffusion during the required measurement time, which is much longer than the coherence time.

Experiments based on third-order signals, such as four–wave mixing in the transient coherent domain after pulsed excitation[24] or spectral hole-burning in the frequency domain with continuous–wave excitation[42] allow one to overcome the presence of an inhomogeneous distribution and can be detected free of backgrounds with appropriate selection in the direction and/or frequency domain. The formal treatment of third–order non-linearities can be found in Ref. 43, and the application to nonlinear optical spectroscopy is given in Ref. 44. The application of transient FWM to the measurement of the dephasing time in semiconductors was recently reviewed in Ref. 45 and 46.

In the following we discuss the properties of transient degenerate three-beam FWM. In this configuration, three exciting pulses are used, spectrally centered at the same optical frequency ω which is usually in resonance with the optical transition of interest. The pulses are described by the complex electric fields $\mathcal{E}_{1,2,3}(t)$ centered at time $t = 0$, and are time-shifted by variable delay times τ_{12} and τ_{13}, resulting in a total exciting field of $\mathcal{E}(t) = \mathcal{E}_1(t) + \mathcal{E}_2(t-\tau_{12}) + \mathcal{E}_3(t-\tau_{13})$. To separate effects of different orders in the incident field amplitude, the population and the polarization described by the diagonal and off-diagonal elements of the density matrix can be expanded into a Taylor series[24,43]. Consequently, the optical Bloch equations separate in a series of equations which can be truncated to a desired order.

In extended media, one can discriminate the different orders experimentally using defined wavevectors (i.e. directions) $\mathbf{k}_{1,2,3}$ of the excitation fields. The $\mathbf{n}$-th order polarization $P^{(\mathbf{n})} \propto \mathcal{E}_1^{n_1}\mathcal{E}_1^{*m_1}\mathcal{E}_2^{n_2}\mathcal{E}_2^{*m_2}\mathcal{E}_3^{n_3}\mathcal{E}_3^{*m_3}$ with $\mathbf{n} = (n_1, m_1, n_2, m_2, n_3, m_3)$, and n_j and m_j natural numbers including zero, emits in the direction $l_1\mathbf{k}_1 + l_2\mathbf{k}_2 + l_3\mathbf{k}_3$ where $l_j = n_j - m_j$. For example, the three-beam FWM signal which has an echo for positive τ_{12} corresponds to $n_1 = 0$, $m_1 = 1$, $n_2 = 1$, $m_2 = 0$,$n_3 = 1$, $m_3 = 0$ and is emitted in the direction $\mathbf{k}_3 + \mathbf{k}_2 - \mathbf{k}_1$, which can be intuitively understood as the direction into which pulse 3 is diffracted by the density grating created due to the interference of the polarization created by pulse 1 with the field of pulse 2. Since phase matching conditions (i.e. energy and momentum conservation) result in a critical thickness for the mixing process to be efficient[43], this directional selection geometry is only suited for thin films, except when using the so-called box-geometry in three-pulse four-wave mixing, which is important to investigate gases or liquids as it allows for thicker specimen. For sub-wavelength sized systems like individual excitonic transitions, or strongly disordered systems, the broken translational invariance prohibits the use of such a wavevector selection. We can however still use the time invariance provided that there is a temporal stability of the investigated structure over the course of the experiment. In this case, the orders of the nonlinear polarization can be discriminated using a frequency selection scheme. In a degenerate resonant case this is obtained by slightly ($\ll \gamma$) shifting the optical frequencies of the pulses, for example by radio-frequency amounts Ω_j using acousto-optic modulators, and by repeating the experiment using pulse trains which then exhibit controlled phase variations given by $\exp(i\Omega_j t)$. Such a frequency selection scheme combined with an interferometric detection of the FWM field amplitude is the essence of the heterodyne detection scheme. A detailed description of this technique can be found in Sec. II B.

The time evolution of the third–order FWM polarization created by $\mathcal{E}(t)$ can be solved analytically assuming delta-like pulses of areas $\mathcal{E}_{10}$, $\mathcal{E}_{20}$, $\mathcal{E}_{30}$ which is a good approximation for pulse durations much shorter than the dephasing time of the optical transition under consideration. For a system described as a two-level optical transition without inhomogeneous broadening and with a single exponential decay of the polarization given by T_2 and a density lifetime of T_1 such a solution is

$$P^{(3)}_{\mathrm{FWM}} \propto \mu^4 \mathcal{E}^*_{10}\mathcal{E}_{20}\mathcal{E}_{30}\theta(\tau_{12})\theta(\tau_{13})\theta(t-\tau_>) \times e^{-g(t-\tau_>)}e^{-|\tau_{23}|\Gamma}e^{-g^*\tau_<}\,, \qquad (5)$$

where $\tau_{23} = \tau_{13} - \tau_{12}$, $\tau_< = \min(\tau_{13}, \tau_{12})$, $\tau_> = \max(\tau_{13}, \tau_{12})$, μ is the projection of transition dipole moment along the field polarization direction (assuming co-polarized exciting fields), $g = i\omega_0 + \gamma$ with the resonance frequency of the two-level transition ω_0, $\Gamma = 1/T_1$, and θ is the Heaviside function. Apart from the oscillatory terms, the polarization decays exponentially with a time constant T_2 both with $\tau_<$ and $t-\tau_>$, and is non-zero only for $\tau_{12} > 0$, $\tau_{13} > 0$ and $t > \tau_>$.

The phase conjugation of the g-terms in Eq.(5) is significant when considering the FWM signal for an inhomogeneously broadened ensemble, i.e. if a distribution of resonance frequencies ω_0 is present. At time $t = \tau_{12} + \tau_{13} = \tau_> + \tau_<$ the exponential term simplifies into $e^{-2\gamma\tau_< - \Gamma|\tau_{23}|}$, and is independent of ω_0. Therefore, the superposition of the third-order polarizations from N two-level systems with frequencies ω_{0_j} creates a constructive interference at this time with a total FWM ampli-

tude N times larger than the individual FWM amplitudes of the single transitions, assuming identical amplitudes of the individual third-order polarizations. For other times, the phases are, in general, randomly distributed due to the distribution of the transition frequencies, and the total FWM amplitude is only about $\sqrt{N}$ times the individual amplitude. For typical ensemble-measurements shown later we have $N \approx 10^5 - 10^8$. In the limit of a large number of systems in the ensemble, the signal at $t = \tau_{12} + \tau_{13}$ is thus far larger than at other times, and is called a photon echo. For large enough N, i.e. $N\gamma \gg \sigma$, we describe the ensemble by a continuous distribution of transition frequencies ω_0' according to the Gaussian

$$G(\omega_0') = \frac{1}{\sigma\sqrt{2\pi}} \exp\left[-\frac{(\omega_0' - \omega_0)^2}{2\sigma^2}\right] \tag{6}$$

where $NG(\omega_0')d\omega_0'$ is the number of systems with transition frequencies between ω_0' and $\omega_0' + d\omega_0'$. The third-order polarization in Eq.(5) summed over the inhomogeneous distribution is then given by

$$\int_{-\infty}^{+\infty} P^{(3)}_{\mathrm{FWM}}(\omega_0', t) NG(\omega_0') d\omega_0' = NP^{(3)}_{\mathrm{FWM}}(\omega_0, t) \exp\left[-\frac{\sigma^2(t - \tau_> - \tau_<)^2}{2}\right], \tag{7}$$

showing that the FWM of a inhomogeneously broadened large ensemble is a photon echo in real time, i.e. it appears as a pulsed signal after a time interval $\tau_<$ from the last exciting pulse. A sketch of the related time evolution is shown in Fig. S4. Note that with similar considerations as for Eq.(7) one can calculate that the time evolution of the *first-order* macroscopic polarization of a inhomogeneously broadened large ensemble is given by the product of an exponential decay of rate γ and a Gaussian decay inversely proportional to the frequency width of the inhomogeneous distribution. Therefore, when $\sigma \gg \gamma$ the dynamics of the macroscopic first-order polarization is dominated by the fast decay from the inhomogeneous broadening and its time-evolution is not a good probe of the dephasing time T_2. Measuring the third-order FWM signal associated with the solution in Eq.(7) overcomes the problem of the inhomogeneous broadening since the photon echo acts as a probe of the homogeneously broadened polarization at the echo time.

B. Heterodyne detection

An arrangement illustrating a heterodyne detection technique which can be used for transient FWM experiments without directional selection, is shown in Fig. S5. The pulse train provided by a mode-locked laser source is divided into the excitation pulses and reference pulses. The spectrum of the pulse train consists of series of longitudinal modes of frequencies separated by the repetition

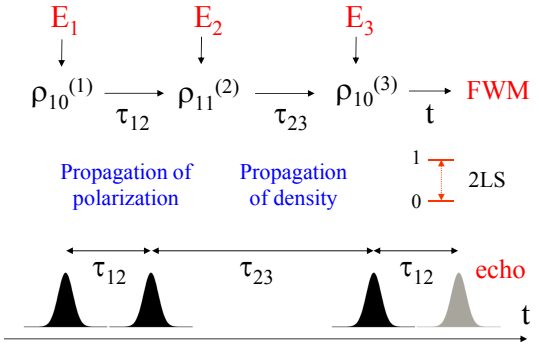

FIG. S4. Sketch of the time-sequence of a three-beam four-wave mixing signal by a two-level system. Top: Pulse sequence and relevant density matrix elements. Bottom: Photon echo formation of the polarization component $\mathcal{E}_1^*\mathcal{E}_2\mathcal{E}_3$ in a inhomogeneously broadened ensemble of two-level systems excited with pulses of a spectral width smaller than the inhomogeneous broadening.

rate. The electric field $E(t)$ of a pulse train with a time period of $T_\mathrm{p} = 2\pi/\Omega_\mathrm{p}$ can be written as a Fourier series[47]

$$E(t) = \mathcal{E}(t) + c.c., \quad \mathcal{E}(t) = e^{-i\omega_0 t} \sum_{n\in\mathbb{Z}} A_n e^{-in\Omega_{\mathrm{rep}} t}. \tag{8}$$

The complex field $\mathcal{E}(t)$ has the Fourier coefficients A_n, with an envelope of $|A_n|^2$ given by the spectrum of a single pulse in the train. In the heterodyne experiment, the excitation pulses are frequency upshifted by $\sim 100\,\mathrm{MHz}$ by acousto–optic modulators (AOM). We assume that the pulse is close to Fourier-limited and that its duration is much smaller than the period of the AOM frequency $2\pi/\Omega_{\mathrm{AOM}}$, i.e. that the spectral width Δ of the envelope of $|A_n|^2$ is much larger than Ω_{AOM}. The complex fields of the reference and signal pulse trains are then given by

$$\mathcal{E}_\mathrm{r}(t) = e^{-i\omega_0(t-\tau_\mathrm{r})} \sum_n A^\mathrm{r}_n e^{-in\Omega_\mathrm{p}(t-\tau_\mathrm{r})} \tag{9}$$

$$\mathcal{E}_\mathrm{s}(t) = e^{-i(\omega_0+\Omega_\mathrm{s})t} \sum_n A^\mathrm{s}_n e^{-in\Omega_\mathrm{p} t} \tag{10}$$

where we assume that the signal to be detected has a frequency shift Ω_s. Each photodiode in the detection scheme generates a photo-current proportional to the square of the incoming field, time-integrated over the response time T_{det} of the diodes. In the balanced detection we measure the photocurrent difference $I_\mathrm{d} = I_\mathrm{b} - I_\mathrm{a}$,

$$I_\mathrm{d} \propto \int_{T_{\mathrm{det}}} dt(E_\mathrm{b}^2 - E_\mathrm{a}^2) \propto \int_{T_{\mathrm{det}}} dt E_\mathrm{r} E_\mathrm{s} = \int_{T_{\mathrm{det}}} dt \Big[e^{-i(2\omega_0+\Omega_\mathrm{s})t + i\omega_0\tau_\mathrm{r}} \sum_{n,m} A^\mathrm{s}_n A^\mathrm{r}_m e^{-i(n+m)\Omega_\mathrm{p} t + im\Omega_\mathrm{p}\tau_\mathrm{r}} + e^{-i\Omega_\mathrm{s} t - i\omega_0\tau_\mathrm{r}} \sum_{n,m} A^\mathrm{s}_n A^{*\mathrm{r}}_m e^{-i(n-m)\Omega_\mathrm{p} t - im\Omega_\mathrm{p}\tau_\mathrm{r}} + c.c. \Big] \tag{11}$$

where Eq.(9) has been used and n, m are integer. The terms in Eq.(11) which are rapidly oscillating with $2\omega_0$ average to zero over $T_{\rm det} \gg 2\pi/\omega_0$. Conversely, terms oscillating at the frequency $\Omega_{\rm s}$ or smaller can be time-resolved by the detector, i.e. $T_{\rm det} < 2\pi/\Omega_{\rm s}$. The lock-in amplifier can then filter the photocurrent oscillating at $\Omega_{\rm s}$, i.e. the terms in Eq.(11) oscillating with $\Omega_{\rm s}$, which are those with $m = n$. Alternatively, the lock-in can filter the signal at sidebands of the laser repetition, i.e. at $\Omega_{\rm s} - p\Omega_{\rm p}$ with p integer. To reach a detection frequency range around one MHz providing low 1/f noise and acoustics, and low radiation pickup, we can arrange that $\Omega_{\rm s}$ is only slightly larger than $\Omega_{\rm p}$ (e.g. 78 MHz and 76 MHz, respectively) and choose $m = n + 1$ for which we have

$$I_{\rm d} \propto e^{-i(\Omega_{\rm s}-\Omega_{\rm p})t} \sum_n A^{\rm s}_n A^{*\rm r}_{n+1} e^{-in\Omega_{\rm r}\tau_{\rm r}} + c.c. \quad . \qquad (12)$$

The integration over $T_{\rm det}$ does not appear in Eq.(12) since the oscillation with frequency $\Omega_{\rm s} - \Omega_{\rm p}$ is slowly varying over $T_{\rm det}$. Note that the $\tau_{\rm r}$-dependent term which multiplies the term $e^{-i(\Omega_{\rm s}-\Omega_{\rm p})t}$ has the form of a Fourier series with the n-th Fourier component being $A^{\rm s}_n A^{*\rm r}_{n+1}$. The previously imposed condition $\Delta \gg \Omega_{\rm AOM}$ implies that we can approximate $A^{*\rm r}_{n+1}$ with $A^{*\rm r}_n$. The resulting term $A^{s}_n A^{*\rm r}_n$ is therefore actually the n-th Fourier component of the cross–correlation $C(\tau_{\rm r})$ between the complex reference and signal fields, so that the sum in Eq.(12) is $C(\tau_{\rm r})$. The selection of the different signals is accomplished by choosing the corresponding detection frequency $\Omega_{\rm d}$, which is used as reference for a dual-phase lock-in measuring the photocurrent, and retrieving both real and imaginary part of $C(\tau_{\rm r})$. The excitation pulses are detected at $\Omega_{\rm d} = \Omega_j - \Omega_{\rm p}$, respectively, and the FWM is detected at $\Omega_{\rm d} = \Omega_3 + \Omega_2 - \Omega_1 - \Omega_{\rm p}$. In choosing the AOM frequencies and the laser repetition rate appropriately we make sure that all these frequencies are well separated, typically by about a MHz. In the reported experiments we used $\Omega_{\rm p}/2\pi = 76.11$ MHz, $\Omega_1/2\pi = 80$ MHz, $\Omega_2/2\pi = 79$ MHz, and $\Omega_3/2\pi = 78.6$ MHz. These result in a FWM detection frequency of $(\Omega_3 + \Omega_2 - \Omega_1 - \Omega_{\rm p})/2\pi = 1.49$ MHz.

C. Optical Setup

The heterodyne detected three-beam four-wave mixing data were taken using the experimental setup shown in Fig. S5. It is the same used in our previous works Ref. 19 and 20. The setup is situated in a temperature stabilized (±1°C) room on an optical table with pneumatic legs, and is encapsulated by a cover to reduce air convection which is required to achieve passive optical phase stability over seconds to minutes. A train of (100 ± 10) fs intensity FWHM pulses with 76 MHz repetition rate is created by intracavity doubling the signal beam of an optical parametric oscillator pumped by a Kerr-lens mode-locked Ti:Sapphire laser pumped by

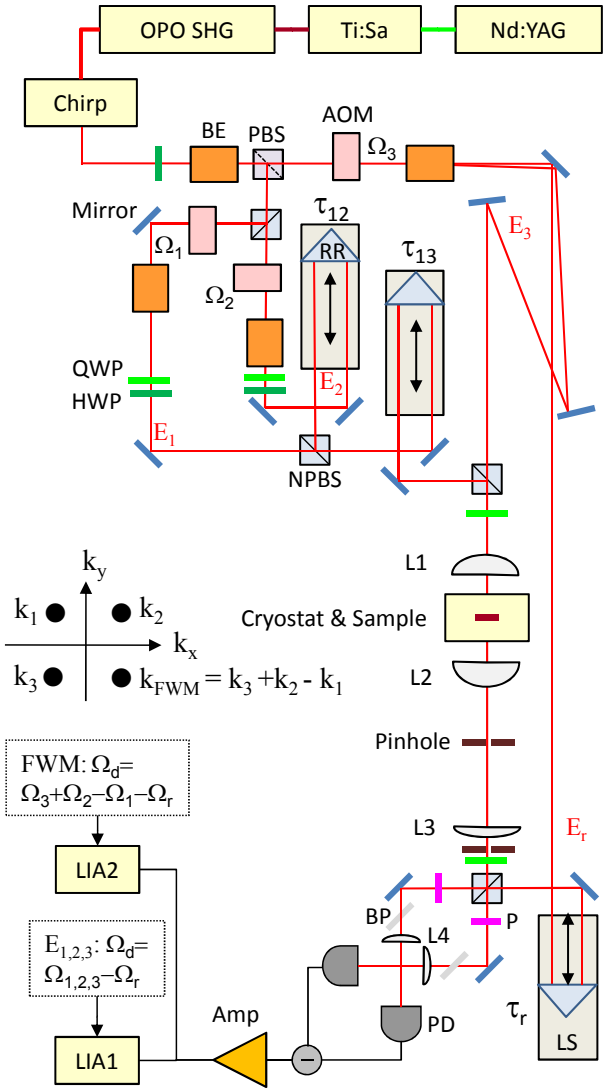

FIG. S5. Sketch of the setup used to measure heterodyne detected four-wave mixing. The individual components are defined in Sec. II C 1.

a intracavity frequency doubled Nd:YAG laser pumped by semiconductor diode lasers. This source can cover a wavelength range from 350 nm to 1.6 μm, and has allowed us to measure a wide range of material systems. Since the optical components, specifically the acousto-optical modulator (AOM), introduce a significant group delay dispersion, we use a grating based pulse shaper to compensate the linear chirp to achieve Fourier-limited pulses at the sample position. This is adjusted using an autocorrelator (AC) of the beam picked up after the AOM. Some of the optical elements in the setup have to be exchanged across the wavelength range of the laser, specifically the beamsplitters (PBS, NPBS), the AOMs, the waveplates (QWP, HWP), and the photodiodes (PD). The elements specified in Section II C 1 refer to the wavelength range around 500 nm used in the present work.

A polarizing beam splitter (PBS) is used to split off

a beam with a splitting ratio adjustable with a half-wave plate (HWP). This beam is further split by a non-polarizing beam splitter into the beams 1 and 2. A beam expander (BE) changes the beam size by a factor of 3/10 and creates a Gaussian tail in all the three AOMs, which are deflecting a part of the beam by Bragg reflection with a frequency shift given by the carrier frequency of the electrical drive $\Omega_{1,2,3}$ and an amplitude given by the amplitude of the electrical drive. The amplitude of the drive is controlled via the analog input of the drivers, which is connected to the analog outputs of the lock-in amplifier and a 5:1 voltage divider able to drive 40 mA current into 50 Ohm input impedance. After the AOM the beam is expanded by a factor of 10/3 back to its original size having a radial field amplitude $\propto \exp(-(r/w_0)^2)$ with the radius r, to provide a sufficiently collimated beam with a Rayleigh length $z_\mathrm{R} = \pi w_0^2/\lambda$. For $w_0 = 1\,\mathrm{mm}$ as used in the setup, we have $z_\mathrm{R} = 6.3\,\mathrm{m}$ for $\lambda = 500\,\mathrm{nm}$, much larger than the maximum path length difference in the setup of about 0.5 m to create the pulse delays. The BEs are also used to adjust the beam divergence. Beam 2 is passed over a delay line controlling τ_{12} made of a linear stage and a corner cube retro-reflector and is then recombined with beam 1. Corner-cubes are used since their reflection direction is opposite to the incoming, independent of their tip-tilt. The divergence of the beam is $\lambda/(\pi w_0) \approx 0.16\,\mathrm{mrad}$, and a typical tip/tilt accuracy of a linear stage is similar, so that using a right-angle mirror, which has the advantage of simplicity and conservation of horizontal and vertical beam polarizations, would produce significant beam pointing errors. A motion of 150 mm corresponds to 1 ns pulse delay, and the unidirectional repeatability of the stages of 1 μm corresponds to 7 fs pulse delay sufficient to resolve the 100 fs pulse duration. The stages have an accuracy of 100 μm per 50 mm travel. The overlap between the photon echo and the reference pulse has therefore a maximum variation of about 1 ps per 200 ps delay. We have found a relative scaling error of about 10^{-3} between the stages, which we corrected, resulting in a remaining variation of only about 300 fs, which is taken into account in the measurement procedure by scanning the reference delay over the nominal photon echo position and fitting the photon echo amplitude as explained later. Both beams 1 and 2 are passed over another delay line controlling τ_{13} with a total range of 2 ns.

The beam transmitted by the first PBS is split by an AOM into the deflected beam 3, and the un-deflected beam which is used as reference beam. Beams 1, 2, and 3 are recombined by a NPBS and focussed by L1 onto the sample, to a Gaussian spot size of $r_0 = f\lambda/(\pi w_0) \approx 7\,\mu\mathrm{m}$ (intensity FWHM is $r_0\sqrt{2\ln 2} \approx 10\,\mu\mathrm{m}$). The polarization of the three beams on the sample is adjusted by waveplates. Beam 3 is horizontally linearly polarized after the PBS, and can be converted to circular polarization rotating the QWP in front of L1. The polarization of beams 1 and 2 is adjusted using the QWP-HWP combinations in their beam paths.

The sample is mounted into a cold finger helium flow cryostat. The NPLs are embedded in a thin polymer film as described in Sec. I C, which is squeezed between two 1 mm thick c-axis cut quartz plates providing a high thermal conductivity. The circular dichroism of quartz along the c-axis leads to the rotation of a linear polarization by about 27 degrees per mm, but does not affect a circular polarization.

The transmitted beam is imaged onto a pinhole by L2 which is blocking spurious reflections, then collimated by L3 and transmitted through a QWP which is converting the circular polarization back to linear polarization. The beam is then spatially selected using an iris aperture, to select the direction of the signal to be detected, and combined in a NPBS with the reference beam, which has an adjustable delay τ_r. The reference beam is spatially and directionally overlapped with the signal beam. The two outputs are then projected onto horizontal polarization by polarizers, and detected by photodiodes. The beam size is adjusted to the active photodiode area by lenses, and the detected currents are equalized to within 10^{-3} relative error by adjusting the rotation of Brewster plates, to suppress common mode noise of the reference beam.

The diodes are reverse biased with opposite voltages yielding opposite photocurrents, which are combined and amplified by a current preamplifier. At a current gain of $10^5\,\mathrm{V/A}$ the amplifier has an input current noise of $2.1\,\mathrm{pA}/\sqrt{\mathrm{Hz}}$ and an input voltage noise of $2.8\,\mathrm{nV}/\sqrt{\mathrm{Hz}}$. At a frequency of 2 MHz and a diode and cable capacity of about 50 pF, the voltage noise corresponds to a current noise of $1.8\,\mathrm{pA}/\sqrt{\mathrm{Hz}}$, resulting in a total current noise of about $3\,\mathrm{pA}/\sqrt{\mathrm{Hz}}$. The 0.3 mW optical power of the reference beam per diode with a quantum efficiency of 0.75 at a wavelength of 500 nm creates a current of 91 μA per diode, resulting in a total shot noise of $\sqrt{2eI} = 7.6\,\mathrm{pA}/\sqrt{\mathrm{Hz}}$. The electronic noise thus contributes less than 10% to the total noise, so that the detection is shot-noise limited. The current amplifier voltage is analyzed by a dual-channel lock-in amplifier at the frequency Ω_d corresponding to the signal to be detected. The input voltage noise of the lock-in is between 4 and $80\,\mathrm{nV}/\sqrt{\mathrm{Hz}}$ depending on the sensitivity setting, well below the preamplifier output noise of $760\,\mathrm{nV}/\sqrt{\mathrm{Hz}}$.

The lock-in reference frequency Ω_d is created by analog mixing of the AOM driver reference outputs with +10dBm level and the laser repetition rate taken from the internal photodiode of the Ti:Sapphire laser. A sketch of the electronic layout is shown in Fig. S6, which provides reference frequencies for two lock-in amplifiers LIA1 and LIA2. The reference outputs of the AOM drivers are first passed through a 30dB attenuator and a 28dB amplifier to provide an additional isolation of about 56dB from back-propagating signals into the AOM driver which can create spurious signals. LIA1 is provided with the selectable reference frequencies of $\Omega_1-\Omega_\mathrm{p}$, $\Omega_2-\Omega_\mathrm{p}$, or $\Omega_3-\Omega_\mathrm{p}$ to detect the transmitted excitation pulses, which allows to determine the excitation pulse arrival times rel-

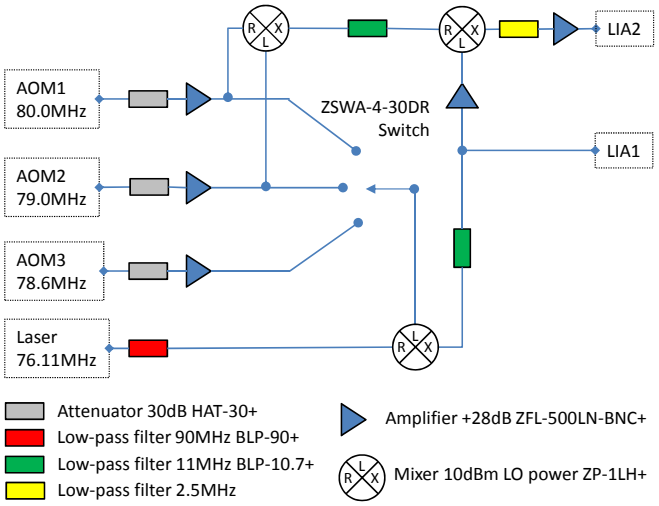

FIG. S6. Sketch of the electronic mixing circuit to create the reference frequency Ω_d for the lock-in. The listed components are from Mini-Circuits except the low-pass filter with 2.5 MHz cutoff frequency which is home build using a 3rd order Butterworth design.

ative to the reference with 10 fs accuracy. These frequencies are created by mixing the low-pass filtered laser photodiode containing only the fundamental frequency, with one of the AOM reference outputs selectable via a switch, and subsequent low-pass filtering to select the difference frequency. LIA2 is provided with the reference frequency $\Omega_3+\Omega_2-\Omega_1-\Omega_p$ to detect the FWM. This is created by first mixing the reference outputs of AOM1 and AOM2 and low-pass filtering to provide the difference frequency $\Omega_1-\Omega_2$. This frequency is then mixed with the reference of LIA1 and low-pass filtered. For a LIA1 reference of $\Omega_3-\Omega_p$ this provides the FWM reference frequency, allowing to measure $\mathcal{E}_3$ and FWM simultaneously.

The setup can be used in collinear geometry, with all beams having the same spatial mode, or in a box geometry indicated in Fig. S5. The former is required for single mode waveguide samples, such as semiconductor optical amplifiers, and has been used by us for a variety of different samples[16,17,48–52]. It is also used for FWM imaging of nanoparticles which we reported in Ref. 53 and 54. However, the collinear geometry has the disadvantage that the detection is exposed to the directly transmitted excitation beams, which can give rise to saturation in the diodes which creates a spurious FWM signal at pulse overlap. When measuring in waveguides, the excitation powers are typically sufficiently small due to the small mode area so that this is not a significant problem. For thin polymer films however, the resonant absorbance is typically below 10% and the spot sizes are larger. In this case the box geometry can be used to select the non-linear signal directionally, suppressing the excitation beam power by typically 2-4 orders of magnitude. The box geometry has been used in the experiments reported in the present work, with a separation between the beams of about 3 mm, corresponding to an angle of about 4 degrees.

1. *Components*

In the following table the main components of the setup shown in Fig. S5 are specified.

Name	Definition	Make
Nd:YAG	cw laser, frequency doubled, diode pumped Nd:YAG laser, power 10 W	Coherent Verdi V10
Ti:Sa	Kerr lens mode locked Ti:Sapphire laser, 100-150 fs pulse duration, power 1.5 W	Coherent Mira 900
OPO SHG	Optical parametric oscillator with intracavity frequency doubling, power 100 mW	APE OPO PP2
Chirp	Grating based pulse shaper for spectral shaping and linear chirp compensation	Home-build
QWP	Achromatic quarter-wave plate	Casix WPA1212 $\lambda/4$ 465-610 nm
HWP	Achromatic half-wave plate	Casix WPA1212 $\lambda/2$ 465-610 nm
PBS	Polarizing cube beamsplitter	Lambda Research Optics BPB-10SF2-550
NPBS	Non-polarizing broadband cube beamsplitter 45%/45%	Lambda Research Optics BNPB-10B-45R-550
BE	Beam expander to reduce beam size to AOM active beam diameter and adjust beam divergence, Galilean f=-30 mm and +100 mm	Casix MgF_2 coated Plano-convex and plano-concave lenses
AOM	Acousto-optic modulator for frequency shifting and intensity control	Intraaction ATM801-A1 & ME-802E6
RR	Retro-reflectors, enhanced aluminium first surface corner cubes	Home-build from Edmund optics NT32-516
LS	Linear stage to change pulse delay, range 150 mm for τ_{12}, 200 mm for τ_r, 300 mm for τ_{13}	Micos VT-80 2SM
P	Glan-Thompson polarizer, to define the detected linear polarization	Casix PGM5210
BP	Brewster plate to fine-tune transmission by rotation to achieve balancing	1 mm thick glass plate cut from microscope slide
PD	Si photodiode, 12 V bias, opposite polarity for current subtraction	Home build using Hamamatsu S7836-01
Amp	Current amplifier, adjustable Gain	Femto DHPCA-100
LIA	Lock-in amplifier, reference frequency Ω_d	Stanford instruments SR844
Pinhole	Pinhole to remove scattered light	200 μm diameter

Name	Definition	Make
L1	Lens to focus beams onto sample, Achromat f=40 mm MgF_2 coated	Casix ACL0201
L2	Lens to image sample onto pinhole, Hastings triplet f=25.4 mm MgF_2 coated	Edmund Optics 30120
L3	Lens to collimate beams from pinhole, plano-convex f=100 mm MgF_2 coated	Casix PCX030
L4	Lens to reduce beam size on diodes, plano-convex f=54 mm MgF_2 coated	
Mirror	Protected silver first surface mirrors $\lambda/10$, 1" diameter	Casix CAG0202
Cryostat	Helium flow coldfinger cryostat, pancake-style	Cryovac KONTI for microscopic measurements
AC	Autocorrelator based on two-photon absorption	APE Mini
Table	Optical table with pneumatic legs	Newport M-RS1000 and I-2000

D. Determination of photon echo amplitude

To determine the photon echo amplitude for given delay times τ_{12} and τ_{13}, the reference delay τ_r is stepped across the echo, and for each τ_r the complex signal S is measured by the dual channel lock-in. Since the signal is phase sensitive, a phase drift during the measurement of ϕ results in a factor on the signal amplitude of $2\sin(\phi/2)/\phi$. To keep the signal reduction below 2%, $|\phi| \lesssim 0.7$, so that the motion of the reference delay stage has to be below $\sim$ 50 nm. To achieve this, we add a delay of about 100 ms after the stage motion is nominally completed before taking data. We use a 24dB filter with a time constant of $\tau_{LI} = 10$ ms. Using this filter results in a rather symmetric temporal response function $\propto t^3 \exp(-t/\tau_{LI})$ and a strong suppression of other components of frequency Ω by $((\Omega - \Omega_s)\tau_{LI} + i)^{-4}$, reaching 8 orders of magnitude at 16 KHz frequency separation, sufficient to suppress the signals of the excitation pulses to below the noise floor. To create a nearly step-like response function suited to take the signal between the movements of τ_r, the signal is read by the PC every 40 ms for 5 times, before the reference delay is moved again, and the average is used as a signal point $S_m(\tau_r)$.

The sampling of the photon echo is adjusted to resolve the photon echo and cover its width, which is given by the laser pulse duration or the inverse inhomogeneous broadening (see Eq.(7)), whichever is longer. In the present case the inhomogeneous broadening is larger than the laser pulses, so that the measured echo is given by the autocorrelation of the laser pulse. We used 7 steps covering the range -300 fs to 300 fs centered at the nominal photon echo position τ_e, which is

$$\tau_e = \begin{cases} \tau_{12} + \tau_{13} & \text{for } \tau_{12} \geq 0 \\ \tau_{13} & \text{for } \tau_{12} < 0 \end{cases}, \tag{13}$$

For $\tau_{12} < 0$, no echo is expected (see Eq.(5)), but due to the finite pulse duration some of the fields still arrive in the correct time ordering.

In order to allow for a large dynamic range in the delay τ_{12} to be covered, we use a delay scan made of two sections. The region of small delays around pulse overlap is covered by N_{lin}+1 equidistant points from τ_{12}^s to τ_{12}^e followed by $N_{log}-1$ points ending at τ_{12}^{log} spaced by equal factors. Explicitly, at the n-th point we set

$$\tau_{12} = \begin{cases} \tau_{12}^s + (\tau_{12}^e - \tau_{12}^s)\frac{n}{N_{lin}} & \text{for } n \leq N_{lin} \\ \tau_{12}^e \exp\left(\frac{n-N_{lin}}{N_{log}} \log\left(\frac{\tau_{12}^{log}}{\tau_{12}^e}\right)\right) & \text{for } n > N_{lin} \end{cases} \tag{14}$$

where $n = 0, 1, .., N_{lin} + N_{log}$. The value of N_{log} is chosen so that the step size is approximately continuous across the junction of the two sections. The data shown in Fig. S7 was taken using τ_{12}^s=-0.3 ps, τ_{12}^e=1 ps, N_{lin}=26, τ_{12}^{log}=250 ps, and N_{log}=113.

In order to retrieve the photon echo amplitude from $S_m(\tau_r)$, we first subtract an offset S_0 which is due to electronic cross-talk from the reference. Then, since the phase of the measured signal is relative to the reference, and the reference phase is not known, we analyze the amplitude of the signal. The noise component S_σ is superimposed on the signal S in S_m, and has an arbitrary phase. The corresponding amplitude square $|S+S_\sigma|^2$ has a noise-averaged value of $|S|^2 + 2\sigma^2$, with the variance of σ of real and imaginary part of S_σ. We therefore calculate the corrected signal amplitude S_c from the measured data S_m using

$$S_c(\tau_r) = \pm\sqrt{\pm|S_m(\tau_r) - S_0|^2 \mp 2\sigma^2}, \tag{15}$$

where the sign is chosen to provide a real result. Both S_0 and σ are determined using the histograms of the measured data in the absence of signal. For the data shown in Fig. S7, we found $\sigma = 1.3\,\mu$V.

Example data of S_c are given in Fig. S7a. $S_c(\tau_r)$ is then fitted by the Gaussian

$$S_e(\tau_r) = \frac{A_e}{w_e\sqrt{\pi/2}} \exp\left(-2\frac{(\tau_r - \tau_e - \tau_0)^2}{w_e^2}\right) \tag{16}$$

with the echo area A_e, the relative center position τ_0, and the width w_e. An example fit is shown in Fig. S7b. The width is expected to be independent of τ_{12}, and therefore it is fixed to the average value found in a preliminary fit. The center position τ_e is kept free within the limits of the data range to account for variations of the relative delay due to the limited positioning accuracy of the linear stages. An example of the fitted values for τ_0 and w_e is given in Fig. S7c). The systematic deviation at delays close to pulse overlap, $\tau_{12} < 0.2$ ps, show the effect of the

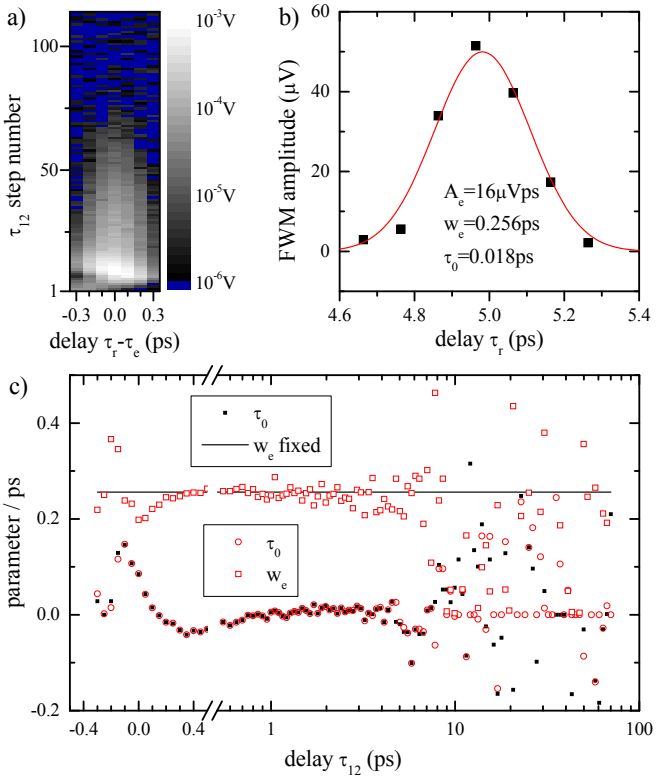

FIG. S7. Photon echo analysis for the data shown in Fig. 2a for T=5 K. a) Measured FWM amplitude $S_c(\tau_r)$ on a logarithmic grey scale as given, for $\tau_{23} = 1$ ps as function of the τ_{12} step number n. Values below 10^{-6} V are shown as blue. b) $S_c(\tau_r)$ for the step $n = 40$, $\tau_{12} = 1.982$ ps, with the Gaussian fit Eq.(16), resulting in the fit parameters as shown. c) Fitted relative position τ_0 (red open circle) and width w_e (red open square), and fitted τ_0 (black square) for constant w_e (black line), as function of τ_{12}.

finite pulse width, The fitted amplitude A_e is used for further analysis, and is plotted in Fig. 2.

For delay scans probing the density dynamics which are not affecting the delay between photon echo and reference, which for the present setup are τ_{13} scans, the reference delay stage is kept fixed and the measured signal $S - S_0$ is directly used, given by the amplitude shown in Fig. 3. In this scan also the phase carries information during the passive phase stability of the setup, and can be used to identify changes of the effect of the density on the susceptibility, which can create both amplitude and phase changes of the transmitted $\mathcal{E}_3$. Measuring both $\mathcal{E}_3$ and FWM at the same time and using an intensity modulation of $\mathcal{E}_1$ instead of the interference of $\mathcal{E}_1$ and $\mathcal{E}_2$, allows to reconstruct the phase of the nonlinear response[55,56].

E. Estimation of the zero-phonon line weight

We estimate the zero-phonon line weight Z from the initial FWM amplitude decay following the procedure

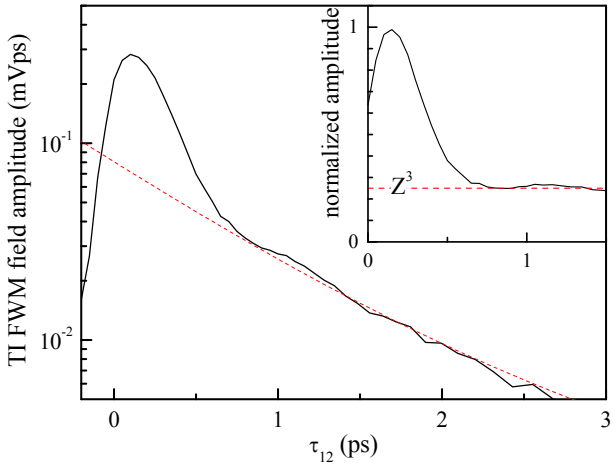

FIG. S8. Measured time-integrated FWM field amplitude at $T = 10$ K together with a double exponential fit of the dynamics at long delay times (γ_2, γ_3 components). The initial FWM dynamics divided by the exponential fit and normalized to the peak, is shown in the inset. The asymptotic value at large delay (dashed line) is given by Z^3.

discussed in Ref. 17. As shown in Fig. S8 using the T= 10 K data of Fig. 2a, the FWM consists of an initial fast decay (the γ_1 component), and a subsequent slower decay (the $\gamma_{2,3}$ components). We attribute the $\gamma_{2,3}$ components to the zero-phonon line, and therefore evaluate Z from the decay of the FWM corrected for the ZPL dynamics, i.e. we divide the measured dynamics by the dynamics of the fitted ZPL components, as shown in the inset. The remaining initial decay is reaching a fraction Z^3 of its peak after the signal of the phonon-assisted transitions has decayed. Above a temperature of 40 K, the dynamic range of the measurements is insufficient (see Fig. 2a) to determine the ZPL component and thus the value of Z.

F. Coherent phonon oscillations

A damped oscillation with a period of about 1 ps is observed in the exciton density decay dynamics in Fig. 3. These oscillations can be assigned to the modulation of the excitonic absorption by the coherent phonons created by the impulsive excitation, and have been previously observed in a variety of structures including CdSe[25,26] and PbS[27] QDs.

Interestingly, varying τ_{12} the visibility of the oscillations can be controlled[25]. Specifically, for $\omega_p\tau_{12} = 0, 2\pi$ ($\tau_{12} \sim 0, 1$ ps), where ω_p is the angular phonon frequency, the oscillations are suppressed, while for $\omega_p\tau_{12} = \pi$ ($\tau_{12} \sim 0.5$ ps) they are enhanced. We have modeled the oscillations in the fit by multiplying the bi-exponential decay by $(1+B\exp(-\gamma_p\tau_{23})\cos(\omega_p\tau_{23}))$ with the phonon decay rate γ_p and the amplitude B.

The complete fit function $S(t)$ to the density dynam-

ics, taking into account a Gaussian excitation pulse of intensity $\propto \exp(-(t/\tau_{\rm ac})^2)$ is then given by

$$S(t) = \sum_{n=1}^{2} A_n \exp\left(\frac{\tau_{\rm ac}^2}{4T_n^2} - \frac{t}{T_n}\right)\left[\frac{1}{e^{\frac{T_{\rm p}}{T_n}}-1} + \frac{1+Be^{-\gamma_{\rm p}t}\cos(\omega_{\rm p}t)}{2}\left(1+\mathrm{erf}\left(\frac{t}{\tau_{\rm ac}}-\frac{\tau_{\rm ac}}{2T_n}\right)\right)\right] \quad (17)$$

with the amplitudes A_n, the exponential time constants T_n, and the pulse repetition period $T_{\rm p}$. The buildup from previous pulses is given by the term $1/(\exp(T_{\rm p}/T_n)-1)$, which is the sum of the geometric series $\sum_{k=1}^{\infty}\exp(-T_{\rm p}/T_n)$.

The fit to the data (see Fig. 3) yields $\hbar\omega_{\rm p} = (4.1 \pm 0.1)\,\mathrm{meV}$ and $\hbar\gamma_{\rm p} = (1.5 \pm 0.2)\,\mathrm{meV}$. The oscillation frequency is similar to the expected frequency of the lowest longitudinal acoustic (LA) phonon mode confined by the NPL thickness given by $\hbar\omega_{\rm p} = hv/(2L_z) = 4.6\,\mathrm{meV}$, with the LA velocity in CdSe $v = 3.7\times10^3\,\mathrm{m/s}$[57]. The in-plane wavevector of the fundamental phonon mode excited by the delocalized exciton density can be neglected since $L_z \ll L_x, L_y$. The mode damping $\gamma_{\rm p}$ expected due to the transmission to the polystyrene environment can be estimated using the amplitude reflection coefficient of $r = 0.75$ of the CdSe/PS interface calculated using the acoustic impedance mismatch, yielding $\hbar\gamma_{\rm p} = \hbar\ln(r)v/L_z = 0.44\,\mathrm{meV}$. This result is significantly smaller than the fitted value, which could be due to an inhomogeneous distribution of oscillation frequencies in the measured NPL ensemble, for example due to the varying coupling to PS considering that L_z corresponds to only 6 styrene ring diameters.

* langbeinww@cardiff.ac.uk

[1] S. Ithurria and B. Dubertret, J. Am. Chem. Soc. **130**, 16504 (2008).
[2] S. Ithurria, M. D. Tessier, B. Mahler, R. P. S. M. Lobo, B. Dubertret, and A. L. Efros, Nat. Mater. **10**, 936 (2011).
[3] M. D. Tessier, C. Javaux, I. Maksimovic, V. Loriette, and B. Dubertret, ACS Nano **6**, 6751 (2012).
[4] K. Leosson, J. R. Jensen, W. Langbein, and J. M. Hvam, Phys. Rev. B **61**, 10322 (2000).
[5] J. Voigt, F. Spiegelberg, and M. Senoner, physica status solidi (b) **91**, 189 (1979).
[6] E. A. Muljarov, S. G. Tikhodeev, N. A. Gippius, and T. Ishihara, Phys. Rev. B **51**, 14370 (1995).
[7] A. Achtstein, A. Schliwa, A. Prudnikau, M. Hardzei, M. Artemyev, C. Thomsen, and U. Woggon, Nano Lett. **12**, 3151 (2012).
[8] A. Chernikov, T. C. Berkelbach, H. M. Hill, A. Rigosi, Y. Li, O. B. Aslan, D. R. Reichman, M. S. Hybertsen, and T. F. Heinz, Phys. Rev. Lett. **113**, 076802 (2014).
[9] L. Biadala, F. Liu, M. D. Tessier, D. R. Yakovlev, B. Dubertret, and M. Bayer, Nano Lett. **14**, 1134 (2014).
[10] J. Feldmann, G. Peter, E. O. Göbel, P. Dawson, K. Moore, C. Foxon, and R. J. Elliott, Phys. Rev. Lett. **59**, 2337 (1987).
[11] L. C. Andreani, G. Panzarini, and J.-M. Gérard, Phys. Rev. B **60**, 13276 (1999).
[12] J. Hours, P. Senellart, E. Peter, A. Cavanna, and J. Bloch, Phys. Rev. B **71**, 161306(R) (2005).
[13] V. Savona and W. Langbein, Phys. Rev. B **74**, 075311 (2006).
[14] P. Borri, W. Langbein, J. M. Hvam, and F. Martelli, Phys. Rev. B **60**, 4505 (1999).
[15] W. Langbein and J. M. Hvam, Phys. Rev. B **61**, 1692 (2000).
[16] P. Borri, W. Langbein, S. Schneider, U. Woggon, R. L. Sellin, D. Ouyang, and D. Bimberg, Phys. Rev. Lett. **87**, 157401 (2001).
[17] P. Borri, W. Langbein, U. Woggon, V. Stavarache, D. Reuter, and A. D. Wieck, Phys. Rev. B **71**, 115328 (2005).
[18] F. Masia, W. Langbein, I. Moreels, Z. Hens, and P. Borri, Phys. Rev. B. **83**, 201309(R) (2011).
[19] F. Masia, N. Accanto, W. Langbein, and P. Borri, Phys. Rev. Lett. **108**, 087401 (2012).
[20] N. Accanto, F. Masia, I. Moreels, Z. Hens, W. Langbein, and P. Borri, ACS Nano **6**, 5227 (2012).
[21] See Supplemental Material for more details on several topics, which also includes Refs. [3457].
[22] I. Fedin and D. V. Talapin, J. Am. Chem. Soc. **136**, 11228 (2014).
[23] P. Borri and W. Langbein, in *Semiconductor Quantum Bits*, edited by O. Benson and F. Henneberger (World Scientific, Singapore, 2009).
[24] J. Shah, "Ultrafast spectroscopy of semiconductors and semiconductor nanostructures," (Springer, Berlin, 1996) Chap. 2.
[25] D. M. Mittleman, R. W. Schoenlein, J. J. Shiang, V. L. Colvin, A. P. Alivisatos, and C. V. Shank, Phys. Rev. B **49**, 14435 (1994).
[26] L. Dworak, V. V. Matylitsky, M. Braun, and J. Wachtveitl, Phys. Rev. Lett. **107**, 247401 (2011).
[27] T. D. Krauss and F. W. Wise, Phys. Rev. Lett. **79**, 5102 (1997).
[28] V. N. Gladilin, S. N. Klimin, V. M. Fomin, and J. T. Devreese, Phys. Rev. B **69**, 155325 (2004).
[29] S. A. Crooker, T. Barrick, J. A. Hollingsworth, and V. I. Klimov, Appl. Phys. Lett. **82**, 2793 (2003).
[30] L. C. Andreani, "Confined electrons and photons: New physics and applications," (Plenum Press, New York, 1995) pp. 57–112.
[31] W. Langbein, C. Mann, U. Woggon, M. Klude, and D. Hommel, phys. stat. sol. (a) **190**, 861 (2002).
[32] H. P. Wagner, A. Schätz, R. Maier, W. Langbein, and J. M. Hvam, Phys. Rev. B **57**, 1791 (1998).
[33] P. R. Dolan, G. M. Hughes, F. Grazioso, B. R. Patton, and J. M. Smith, Opt. Lett. **35**, 3556 (2010).
[34] M. D. Tessier, L. Biadala, C. Bouet, S. Ithurria, B. Abecassis, and B. Dubertret, ACS Nano **7**, 3332 (2013).
[35] R. F. Schnabel, R. Zimmermann, D. Bimberg, H. Nickel, R. Lösch, and W. Schlapp, Phys. Rev. B **46**, 9873 (1992).
[36] A. Pasquarello and L. C. Andreani, Phys. Rev. B **44**, 3162 (1991).

[37] W. Langbein, J. M. Hvam, and R. Zimmermann, Phys. Rev. Lett. **82**, 1040 (1999).
[38] G. Kocherscheidt, W. Langbein, G. Mannarini, and R. Zimmermann, Phys. Rev. B **66**, 161314(R) (2002).
[39] D. Gammon, E. S. Snow, B. V. Shanabrook, D. S. Katzer, and D. Park, Science **273**, 87 (1996).
[40] M. Bayer and A. Forchel, Phys. Rev. B **65**, 041308(R) (2002).
[41] A. Muller, E. B. Flagg, P. Bianucci, X. Y. Wang, D. G. Deppe, W. Ma, J. Zhang, G. J. Salamo, M. Xiao, and C. K. Shih, Phys. Rev. Lett. **99**, 187402 (2007).
[42] W. Demtröder, *Laser Spectroscopy* (Spinger-Verlag, Berlin, 1998).
[43] Y. R. Shen, *The Principles of Nonlinear Optics* (Wiley-Interscience, New York, 1984).
[44] S. Mukamel, *Principles of Nonlinear Optical Spectroscopy* (Oxford, USA, 1999).
[45] S. T. Cundiff, Opt. Express **16**, 4639 (2008).
[46] W. Langbein, Rivista del nuovo cimento **33**, 255 (2010).
[47] A. E. Siegman, *Lasers* (Oxford, 1986).
[48] W. Langbein, P. Borri, U. Woggon, V. Stavarache, D. Reuter, and A. D. Wieck, Phys. Rev. B **69**, 161301(R) (2004).
[49] V. Cesari, W. Langbein, and P. Borri, Appl. Phys. Lett. **94**, 041110 (2009).
[50] W. Langbein, V. Cesari, F. Masia, A. B. Krysa, P. Borri, and P. M. Smowton, Appl. Phys. Lett. **97**, 211103 (2010).
[51] P. Borri, V. Cesari, and W. Langbein, Phys. Rev. B **82**, 115326 (2010).
[52] V. Cesari, W. Langbein, and P. Borri, Phys. Rev. B **82**, 195314 (2010).
[53] F. Masia, W. Langbein, and P. Borri, Appl. Phys. Lett. **93**, 021114 (2008).
[54] F. Masia, W. Langbein, P. Watson, and P. Borri, Opt. Lett. **34**, 1816 (2009).
[55] F. Masia, W. Langbein, and P. Borri, Phys. Rev. B **85**, 235403 (2012).
[56] F. Masia, W. Langbein, and P. Borri, Phys. Chem. Chem. Phys. **15**, 4226 (2013).
[57] S. Adachi, ed., *Handbook on Physical Properties of Semiconductors*, Vol. 3 (Kluwer Academic, 2004).